CFD Simulations of the IHF Arc-Jet Flow: 9-Inch Nozzle, Flow Surveys, LEAF Wedge Calibration Data

Tahir Gökçen[1] and Antonella I. Alunni[2]
AMA Inc., NASA Ames Research Center, Moffett Field, CA 94035

This paper reports computational analyses and flow characterization studies in a high enthalpy arc-jet facility at NASA Ames Research Center. These tests were conducted using a wedge model placed in a free jet downstream of new 9-inch diameter conical nozzle in the Ames 60-MW Interaction Heating Facility. Both the nozzle and wedge model were specifically designed for testing in the new Laser-Enhanced Arc-jet Facility. Data were obtained using stagnation calorimeters and wedge models placed downstream of the nozzle exit. Two instrumented wedge calibration plates were used: one water-cooled and the other RCG-coated tile plate. Experimental surveys of arc-jet test flow with pitot and heat flux probes were also performed at three arc-heater conditions, providing assessment of the flow uniformity and valuable data for the flow characterization. The present analysis comprises computational fluid dynamics simulations of the nonequilibrium flowfield in the facility nozzle and test box, including the models tested, and comparisons with the experimental measurements. By taking into account nonuniform total enthalpy and mass flux profiles at the nozzle inlet as well as the expansion waves emanating from the nozzle exit and their effects on the model flowfields, these simulations approximately reproduce the probe survey data and predict the wedge model surface pressure and heat flux measurements.

I. Nomenclature

c_i	=	species mass fraction for species i
D_e	=	nozzle exit diameter, cm (or in)
h	=	enthalpy, MJ/kg
h_o	=	total enthalpy, MJ/kg
h_{ob}	=	mass-averaged total enthalpy (or bulk enthalpy), MJ/kg
h_{ocl}	=	centerline total enthalpy, MJ/kg
I	=	arc current, A
M	=	Mach number
M_e	=	Mach number at the boundary layer edge
$\dot{m}$	=	total mass flow rate, g/s
$\dot{m}_m$	=	arc heater main air flow rate, g/s
$\dot{m}_a$	=	add-air flow rate or cold-gas injection rate at the plenum, g/s
$\dot{m}_{ar}$	=	argon flow rate, g/s
p	=	pressure, kPa
p_{box}	=	test box pressure, torr
p_{ch}	=	arc-heater pressure, kPa
p_o	=	total pressure, kPa
p_s	=	surface pressure, kPa
p_{t2}	=	pitot pressure or model stagnation pressure, kPa
$p_1 - p_3$	=	pressure gages on the water-cooled calibration plate (Fig. 2a)
$Q_1 - Q_6$	=	heat flux gages on the water-cooled calibration plate (Fig. 2a)
q_{CWFC}	=	cold-wall full-catalytic heat flux, W/cm^2
q_{HWFC}	=	hot-wall full-catalytic heat flux (radiative equilibrium), W/cm^2

[1] Senior Research Scientist, MS 230-2, Associate Fellow AIAA
[2] Research Scientist, MS 234-1, Member AIAA (currently, Systems Engineer, TSS Branch)

q_{RCG} = hot-wall heat flux computed using RCG surface kinetics, W/cm^2
q_s = surface heat flux, W/cm^2
Re_θ = Reynolds number based on momentum thickness, $\rho_e u_e \theta/\mu_e$
Re_x = Reynolds number based on arc length from the nose, $\rho_e u_e x/\mu_e$
r_c = wedge or model corner radius, m
r_n = nose radius, m
s = arc-length coordinate or the survey probe location, m
T = temperature or translational-rotational temperature, K
T_{RCG} = surface temperature computed using RCG surface kinetics, K
T_v = vibrational-electronic temperature, K
T_s = surface temperature, K
TC_1–TC_{17} = surface thermocouples on the RCG tile calibration plate (Fig. 2b)
V = arc voltage, V
x_{ml} = model location from the nozzle exit plane, cm
δ = boundary layer thickness, cm
ε = hemispherical emissivity, 0.89
μ_e = mixture viscosity at the boundary layer edge, Pa.s
θ = boundary layer momentum thickness, cm
ρ_e = density at the boundary layer edge, kg/m^3
τ_s = surface shear, Pa

II. Introduction

Arc-jet facilities provide the primary means to study the performance of various types of thermal protection systems (TPS) used on the outer surfaces of spacecraft in an aerothermodynamic heating environment. In a high enthalpy arc-jet facility, a test gas, usually air or a mixture of nitrogen, oxygen and argon, is passed through an electric arc discharge where the energy is added to the flow. The test gas is then expanded through a converging-diverging nozzle into an evacuated test chamber to produce high-enthalpy supersonic or hypersonic flow. NASA Ames Research Center (ARC) has four arc-jet facilities within its Arc-Jet Complex [1]. One of these arc-jet facilities, the Interaction Heating Facility (IHF) has recently been upgraded to include a radiative heating capability using high-power fiber lasers [2]. The new Laser-Enhanced Arc-jet Facility (LEAF) is intended to simulate the combined radiative and convective heating environments of the Orion spacecraft heatshield. A new 9-inch conical nozzle and a new wedge model to accommodate panel test articles are designed for testing in the LEAF. Although laser-enhanced heating capability is not limited to the 9-inch nozzle, initial wedge calibration tests were performed in this nozzle. Also, surveys of arc-jet test flow with pitot and heat flux probes were performed for flow characterization.

In support of these tests, computational fluid dynamics (CFD) simulations are used to characterize the arc-jet test environment and its parameters consistent with the facility and calibration measurements and to provide surface quantities and input for material thermal response analyses. The primary objective of the paper is to report these CFD simulations. The present analysis comprises computational Navier-Stokes simulations of the nonequilibrium flowfield in the facility nozzle and test box as well as the flowfield over the models, and comparisons with the calibration measurements and survey data.

III. Arc-Jet Facility and Tests

The Interaction Heating Facility (IHF) at NASA ARC consists of a constricted arc heater, a 60-MW DC power supply, interchangeable conical and semi-elliptical nozzles, a test chamber, and supplementary systems including steam ejector vacuum system, cooling-water system and data acquisition system. The IHF is designed to operate with a set of conical nozzles or a semi-elliptical nozzle at total pressures of 1-9 atm and total bulk enthalpies of 2-28 MJ/kg (air) [3]. The 60-MW constricted arc heater produces high-temperature test gas for both nozzle configurations. The conical nozzle configurations of the IHF are suitable for tests of stagnation coupon and blunted wedge models in hypersonic flow, while the semi-elliptical nozzle configuration is designed mainly for testing flat panels in hypersonic boundary-layer heating environments. Figure 1 shows a schematic diagram of the IHF with its interchangeable nozzles and a photograph of a wedge test in the IHF 9-inch nozzle.

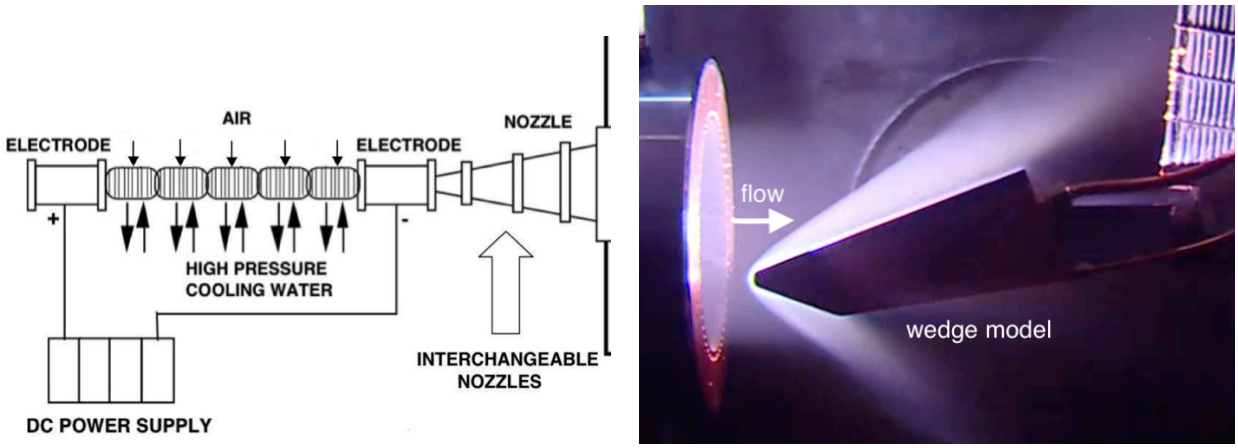

(a) IHF arc-heater/nozzles sketch **(b) LEAF wedge model test**

Figure 1. IHF sketch and a photograph of a wedge test in the IHF 9-inch nozzle.

The IHF 9-inch conical nozzle, like the other IHF conical nozzles, has a throat diameter of 6.033 cm (2.375 in) and the same 10° half-angle for the diverging section, and it has an exit diameter of 22.86 cm (9 in). The new wedge model was specifically designed for testing in the LEAF combined heating environment. It has a 20° half-angle, a nose radius of 0.95 cm (0.375 in), and 22.1 cm width. The wedge model is made of copper and water-cooled, and it can accommodate either a calibration plate or a TPS sample plate size of 15.24 cm x 15.24 cm (6 in x 6 in) for testing.

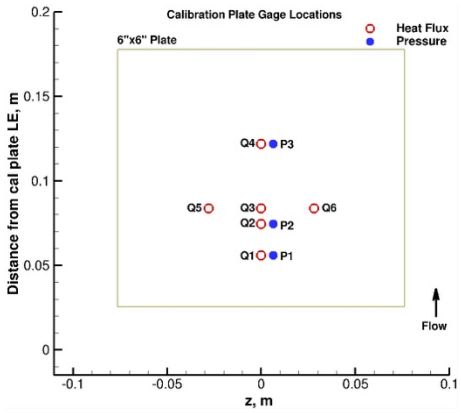

(a) wedge model, water-cooled calibration plate

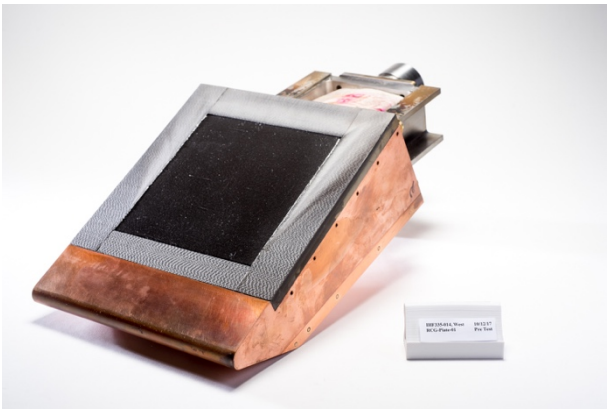

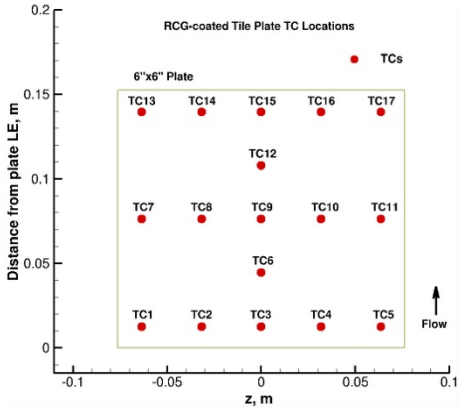

(b) wedge model, RCG-coated tile plate

Figure 2. Photographs of the 8.7-in LEAF wedge models in calibration and test article configurations, and sensor locations on each calibration plate.

Figure 2 shows photographs of the two wedge models, one mounted with a water-cooled calibration plate and the other with the RCG-coated tile plate in test article configuration, including sensor locations on each plate. The water-cooled calibration plate is instrumented with 6 Gardon gage calorimeters and 3 pressure transducers, and the RCG tile plate is instrumented with 17 near-surface thermocouples [2].

For the present paper, while analyses of the LEAF wedge tests conducted using the IHF 9-inch nozzle, designated as IHF 335 test series, are of primary interest, analyses of the nozzle flowfield surveys conducted earlier (IHF 327 tests) are also considered.

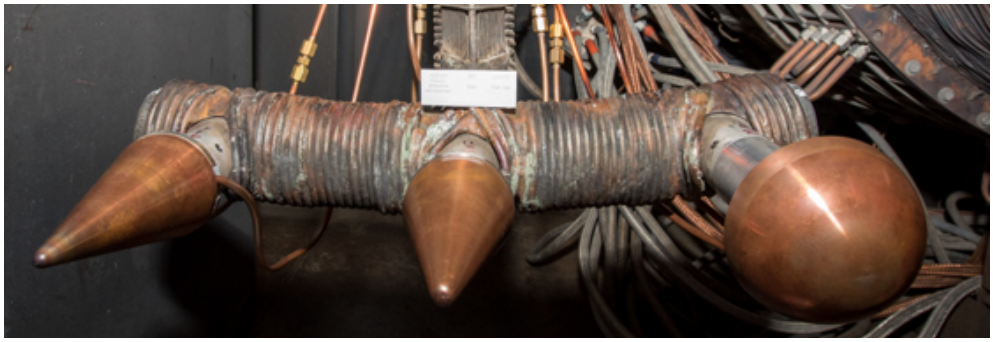

Figure 3. A photograph of the survey probes used to sweep the flowfield of the IHF 9-inch nozzle jet.

In IHF 327 test series, surveys of arc-jet test flow with pitot and heat flux probes were performed for flow characterization. The probe surveys of the nozzle jet in the test section were done at the same or similar arc-heater conditions and at various distances from the nozzle exit. The heat flux surveys presented in this paper were performed with the 15° sphere-cone stagnation probe (r_n = 6.35 mm or 0.25 in), or the 12.7-mm diameter sphere-cone probe. The heat flux probes included coaxial thermocouple sensors. The pitot pressure probe used was a 9.1-mm diameter sphere cone (r_n = 4.57 mm or 0.18 in). Figure 3 shows a photograph of the trident with three survey probes. Note that the trident also includes a 10.16-cm hemisphere calorimeter with a coaxial thermocouple gage, from which the survey data are not considered here because its size is deemed to be too big for this nozzle size to provide spatial resolution for any flow features. The sweeps to survey across the nozzle are obtained as the probes are traversed across the supersonic jet. The probes do not move horizontally or vertically across the jet, but rather follow an arc path with a radius of 139.7 cm (since they are attached to a swing arm). For each survey, first, they move in a forward sweep passing through the nozzle centerline, then they retract back in a backward sweep. This provides two experimental data sets for each survey sweep. Further information on the survey probes and heat flux measurement techniques can be found in [4, 5].

IV. Computational Approach

Computational analyses of arc-jet tests are performed through simulation of nonequilibrium expanding flow in the arc-jet nozzle and supersonic jet, and simulation of the flow in the test box and around the test articles. For all CFD calculations, the Data Parallel Line Relaxation (DPLR) code [6, 7], a NASA Ames in-house flow solver, is used. DPLR has been employed extensively at Ames for hypersonic flight, planetary entry and arc-jet simulations. DPLR provides various options for thermophysical models and formulation. For CFD calculations presented in this paper, two-dimensional axisymmetric or three-dimensional Navier-Stokes equations, supplemented with the equations accounting for nonequilibrium kinetic processes, are used in the formulation. The thermochemical model employed for the arc-jet flow includes six species (N_2 O_2, NO, N, O, Ar), and the thermal state of the gas is described by two temperatures (translational-rotational and vibrational-electronic) within the framework of Park's two-temperature model [8].

The flowfield in an arc-jet facility, from the arc heater to the test section, is a very complex, three-dimensional flow with various nonequilibrium processes occurring. In order to simulate the flowfield, several simplifying assumptions are made, and corresponding numerical boundary conditions are prescribed for CFD simulations. The present computational approach follows our earlier work [9-12], and it is also briefly described here.

Simulations of the arc-jet facility flow are started from the nozzle inlet. The total enthalpy and its radial profile at the inlet are prescribed based on the facility and calibration data, and the flow properties at the inlet are assumed to be in thermochemical equilibrium. Measured facility data, namely, the total pressure, mass flow rate, and test box pressure, are used as boundary conditions. The calibration data obtained include stagnation calorimeter heat flux and pressure in the freestream, pressure and heat flux measurements on the water-cooled wedge calibration plate, and surface thermocouple data on an RCG-coated tile plate. All metallic surfaces, water-cooled nozzle walls, and calorimeter model and calibration plate surfaces (copper slug or Gardon gages), are assumed to be fully catalytic to recombination reactions of atomic oxygen and nitrogen at a constant temperature of 500 K. For the RCG-coated tile plates, surface catalytic efficiency expressions developed by Stewart [13] are prescribed, and surface temperatures are calculated using the radiative equilibrium boundary condition ($\varepsilon = 0.89$). The test box is included in the CFD simulations, primarily to account for the free jet expansion formed by the under-expanded flow exiting the nozzle to the test box and its potential effects on model flowfields. The jet expansion within the test box is primarily determined by the test box static pressure, which is one of the facility measurements and is prescribed as a boundary condition.

V. Computational Results

First, as an example, CFD simulations of the IHF 9-inch nozzle/test box flowfield with a calorimeter model are presented. Second, comparisons of CFD simulations with the pitot and heat flux survey data are given. Finally, the simulation results for the wedge model with the two calibration plate configurations follow, including comparisons with the test data.

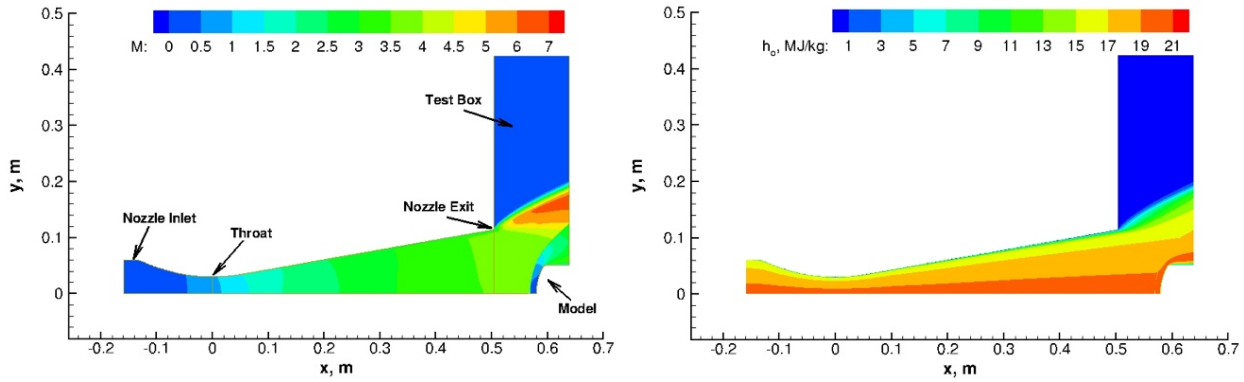

(a) Mach number **(b) total enthalpy**

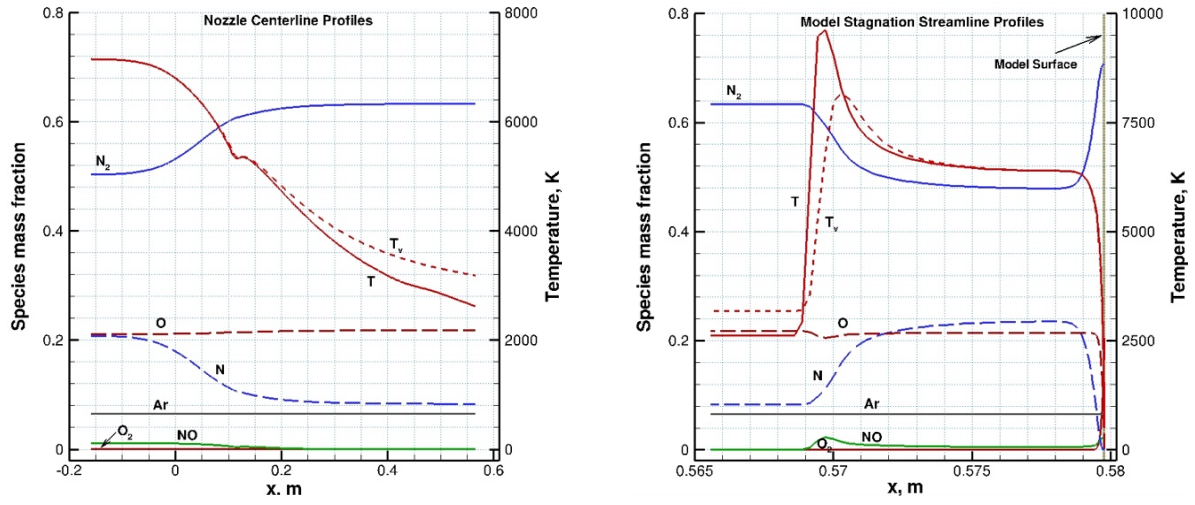

(c) species mass fraction and temperature profiles

Figure 4. Computed IHF 9-inch nozzle flowfield including the test box and a 10.16-cm diameter iso-q model: $\dot{m}$ = 642 g/s, h_{ob} = 17.3 MJ/kg, h_{ocl} = 19.4 MJ/kg, parabolic enthalpy profile, 6.5% Ar, p_{box} = 2 torr.

A. Stagnation calorimeter model simulations

As an illustration of a typical axisymmetric simulation, Fig. 4 shows a computed IHF 9-inch nozzle flowfield including the test box and an iso-q stagnation calorimeter model. Stagnation calorimeters are used to calibrate the test conditions, and to infer the centerline total enthalpy of the arc-jet flow. Figure 4 provides some insight into the arc-jet flowfield chemistry in the nozzle and test box. Because of the nonequilibrium expansion process in arc-jet nozzles, the chemical composition freezes near the throat where the flow is dissociated and vibrationally excited. As shown in Fig. 4c, for this case, the computations predict that the flow is chemically frozen but remains in vibrational nonequilibrium before it reaches the nozzle exit. Note that oxygen remains fully dissociated within the entire flowfield except in the boundary layer near the walls, while nitrogen is partially dissociated.

The primary objective of the stagnation model calculations is to estimate the centerline total enthalpy of the arc-jet flow consistent with the facility and calorimeter measurements. For CFD simulations, uniform pressure and a non-uniform parabolic enthalpy profile are specified at the nozzle inlet such that the centerline calibration data are reproduced with the computations. It is important to reproduce both measured surface pressure and heat flux with CFD simulations in order to estimate the centerline total enthalpy. Note that the estimation of centerline total enthalpy from CFD simulations this way is analogous to the ASTM standard E637-05 [14], except that the calorimeter surface heat flux and pressure are predicted by CFD simulations, replacing the heat transfer theory used in the standard.

As stated earlier, each wedge test included measurements of heat flux and pressure on a water-cooled calibration plate. The CFD-estimated centerline enthalpies inferred from the stagnation calorimeter data are further refined to best reproduce both calorimeter and calibration plate data, provided that these adjustments are within the facility data constraints and their measurement uncertainties. Since the wedge CFD simulations provide estimates of various surface and flow quantities not measured such as surface shear, boundary layer thickness and boundary layer edge Mach number, the reliability of these estimates depends on how well the CFD simulations reproduce the measured quantities.

B. Comparisons with pitot pressure and heat flux survey data

Comparisons of CFD simulations with the survey data follows the approach presented in [10, 11]. While the data obtained from the pitot pressure surveys are used as quantitative data, the heat flux measurements from the coaxial heat flux gage surveys are used as qualitative data since they were not consistent with the slug calorimeter data. Therefore, only normalized distributions of the heat flux measured by the survey probes are used in comparisons with computations. Furthermore, since direct comparisons would require three-dimensional CFD simulations of flowfields around the survey probes at several locations in the test section, only approximate comparisons are made based on the computed axisymmetric CFD flowfields. Quantitative pitot pressure comparisons are based on the CFD flowfield and shock relations (pressure, Mach number, frozen flow). For normalized heating distribution comparisons, the heat flux

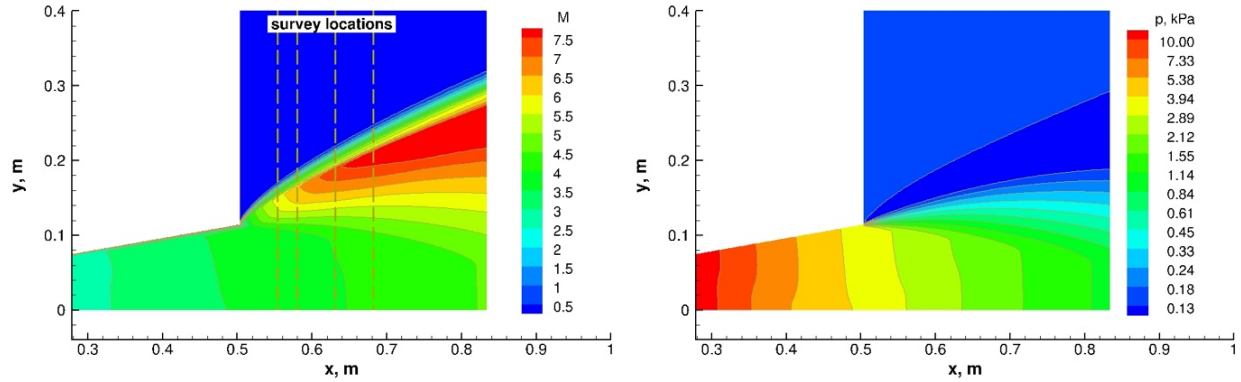

(a) Mach number **(b) pressure**

Figure 5. Computed flowfield contours near the nozzle exit and test box, and four axial locations for the survey probes. IHF 9-inch nozzle flow: $\dot{m}$ = 642 g/s, h_{ob} = 17.3 MJ/kg, h_{ocl} = 19.4 MJ/kg, parabolic enthalpy profile, 6.5% Ar, p_{box} = 1 torr.

from the coaxial gage probes is assumed to be proportional to $h_o p_{t2}^{1/2}$, and corresponding computations are based on the CFD flowfield.

Figure 5 shows the computed Mach number and pressure contours near the nozzle exit and supersonic jet for the case shown in Fig. 4. These simulations do not include the model in the test box. It should be noted that the expansion of the jet exiting the nozzle and the width of the jet is controlled by the test box pressure [15]. On the Mach number contour plot, four survey locations are also indicated. The axial locations for the survey probes are approximately at x = 0.554, 0.580, 0.631, 0.682 m or at x_{ml} = 5.08, 7.62, 12.70, and 17.78 cm (2, 3, 5, and 7 inches downstream of the nozzle exit).

Comparisons of computations with the IHF 327 survey data will be presented for three conditions. Summaries of the facility parameters for the three conditions are listed in Table 1. IHF 327 conditions 1 and 3 (Runs 6-1 and 6-3) are chosen because the arc heater parameters for these are similar to two conditions used in IHF 335 wedge tests. IHF 327 condition 2 (Run 6-2) is chosen because IHF 327 tests included additional runs and the surveys taken at other axial locations shown in Fig. 5a. Note that for all conditions the probe survey data are available at the x_{ml} = 5.08 cm location, which was the wedge model leading edge location for IHF 335 tests.

Table 1. Summary of facility conditions for heat flux and pitot pressure surveys and stagnation calorimeter data obtained in the IHF 9-inch nozzle at x_{ml} = 5.08 cm.

	IHF 327 Tests Facility/Calibration Data		
	Run 6-1	**Run 6-2**	**Run 6-3**
p_{ch}, **kPa**	98	568	815
I, **A**	1948	3431	5945
V, **V**	1886	5847	6611
$\dot{m}$, **g/s**	144	642	849
$\dot{m}_m$	80	545	740
$\dot{m}_a$	50	55	55
$\dot{m}_{ar}$	14	42	54
h_{ob} *(W)*, **MJ/kg**	8.8	16.9	20.8
q_{isoq}, **W/cm²**	207	604	1165
p_{isoq}, **kPa**	9.8	52.8	80.2

The facility bulk enthalpy estimates, $h_{ob(W)}$, are determined by the equilibrium sonic flow method of Winovich [16].

Condition 1, IHF 327: Minimum arc current, low mass flow rate with cold-gas injection

This facility condition represents a relatively low mass flow rate at minimum arc current, and it includes cold-gas injection at the plenum. Even though the cold-gas injection is at the minimum level for the facility, it represents a significant fraction of the total mass flow rate for this condition.

Figure 6 shows the comparisons of computations with the pitot pressure and coaxial-gage heat flux survey data at the x_{ml} = 5.08 location. Note that while the obtained sweep data, both pitot pressure and heat flux data, are mostly repeatable in both sweep directions, they show some asymmetry with respect to the nozzle centerline. Both measured pitot pressure data and corresponding computations show a lower pressure region near the nozzle centerline. Although the measured pressures are slightly asymmetric, the lower pressure region is a result of a small disturbance in the nozzle flowfield caused by the IHF conical nozzle throat design. However, the observed asymmetry is more pronounced in the heat flux survey data. For this condition, aside from the asymmetry, the observed heating distribution appears to be less peaked than computations.

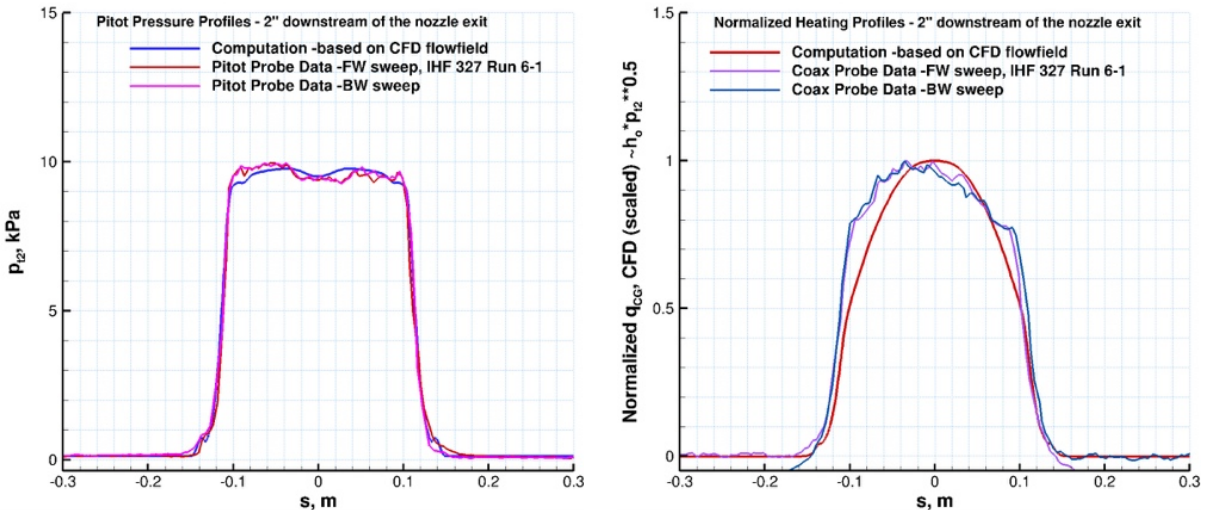

(a) pitot pressure **(b) normalized heat flux**

Figure 6. Comparisons of computations with the pitot pressure and coaxial gage heat flux survey data at x_{ml} = 5.08 cm location. IHF 9-inch nozzle flow: $\dot{m}$ = 144 g/s, h_{ob} = 10.1 MJ/kg, h_{ocl} = 15.4 MJ/kg, parabolic enthalpy profile, 9.7% Ar, p_{box} = 0.5 torr.

Condition 2, IHF 327: Moderate arc current and mass flow rate with minimal cold-gas injection

This facility condition represents an intermediate mass flow rate at moderate arc current, and it includes minimal cold-gas injection at the plenum. Figure 7 shows the comparisons of computations with the pitot pressure and coaxial-gage heat flux survey data at four survey locations, at x_{ml} = 5.08, 7.62, 12.70, and 17.78 cm (2, 3, 5, and 7 inches downstream of the nozzle exit). Note that the survey data were obtained in separate arc-jet runs (runs 6-2, 7-2, 8-2 and 9-2) but at the same nominal facility condition of run 6-2 in Table 1. There appears to be some variation in the pitot pressure measurements near the nozzle centerline, possibly resulting from weak wave interactions in the supersonic jet. The disturbance seen in the surveys is more pronounced at locations closer to the nozzle exit, although present in the pressure survey at the x_{ml} = 17.78 cm location as well. Also, repeatability in the heat flux survey data between the forward and backward sweeps at these locations (x_{ml} = 5.08 and 7.62 cm or 2 and 3 in) is qualitatively not as good as at the locations further downstream. Although the source of this disturbance is not known, the flow disturbance appears to be not axisymmetric. Therefore, it is unlikely that it is originating from the IHF conical nozzle throat design as in the previous case. Except for this disturbance, all of the survey data for this condition, pitot pressure and heat flux, appear to be approximately symmetric, and they are reasonably well reproduced by the CFD simulations.

Condition 3, IHF 327: Maximum arc current and mass flow rate with minimal cold-gas injection

This condition is near the facility maximum in terms of arc heater mass flow rate and arc current, and it includes minimal cold-gas injection at the plenum as well. Figure 8 shows the comparisons of computations with the pitot pressure and coaxial-gage heat flux survey data for another condition. For this case, the surveys are also obtained at only one survey location, x_{ml} = 5.08 cm (or 2 inches downstream of the nozzle exit). The repeatability in the heat flux survey data between the forward and backward sweeps is worse than the previous case. The pitot pressure data show a small dip near the nozzle centerline, similar to the disturbance near the nozzle centerline observed for condition 2. It should be mentioned that for all the wedge tests to be presented shortly, the model leading edge location was x_{ml} = 5.08 cm.

In arc-jet simulations, a nonuniform enthalpy profile is usually needed to be consistent with the mass-averaged (or bulk) facility parameters, namely, mass flow rate and bulk enthalpy. However, in order to use any specific enthalpy profile at the nozzle inlet, some experimental justification is needed. Although there is no single enthalpy profile that can be used for all arc-jet conditions, a parabolic enthalpy profile, with different centerline-to-bulk enthalpy ratios depending on the facility data, is found to be adequate to reproduce available survey data obtained at one or multiple locations downstream of the nozzle exit. The comparisons with the survey data presented here provide additional justification and support the approach used in our earlier work [10-12].

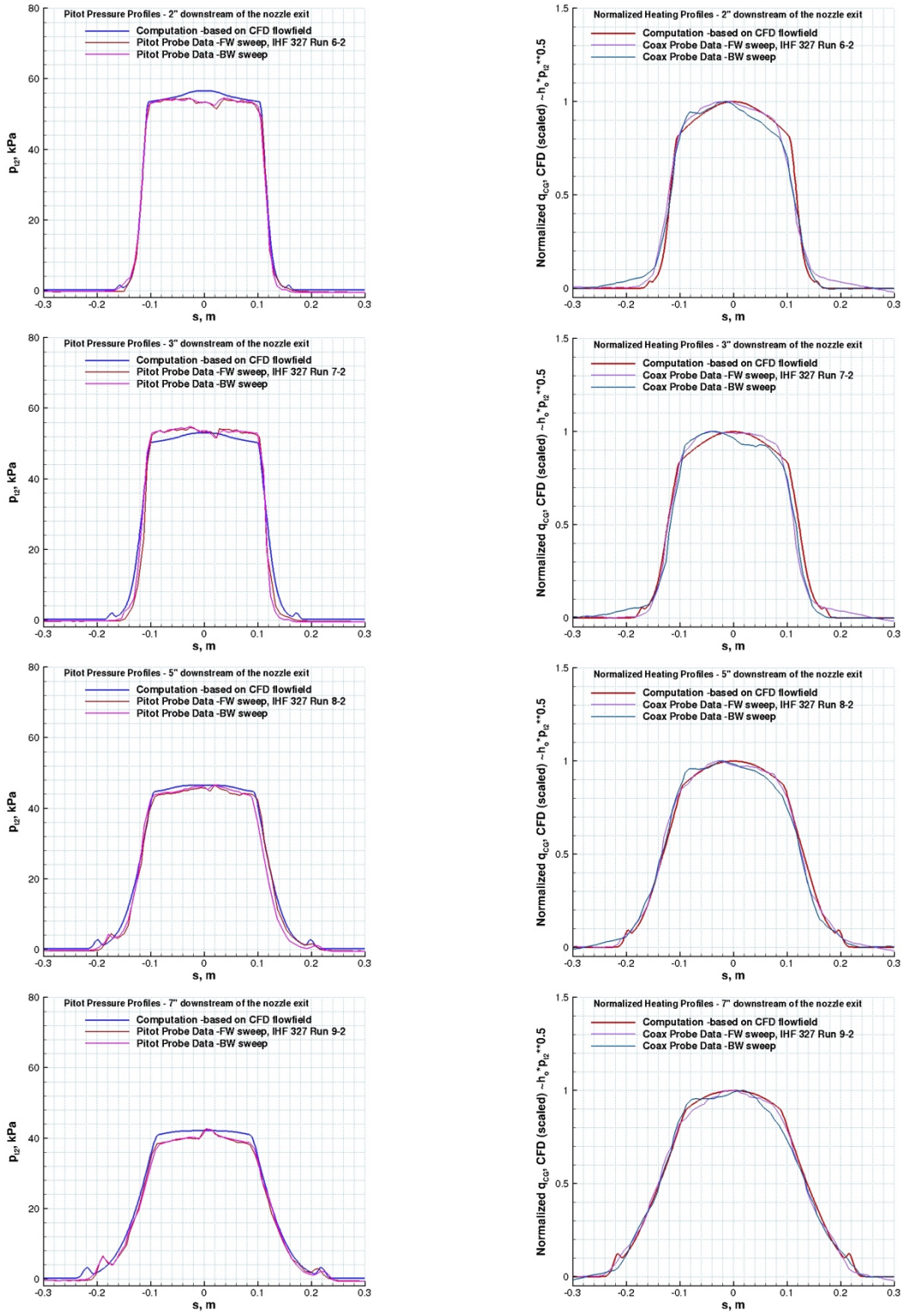

(a) pitot pressure **(b) normalized heat flux**

Figure 7. Comparisons of computations with the pitot pressure and coaxial gage heat flux survey data at four locations (x_{ml} = 5.08, 7.62, 12.70, and 17.78 cm). IHF 9-inch nozzle flow: $\dot{m}$ = 642 g/s, h_{ob} = 17.3 MJ/kg, h_{ocl} = 19.4 MJ/kg, parabolic enthalpy profile, 6.5% Ar, p_{box} = 1 torr.

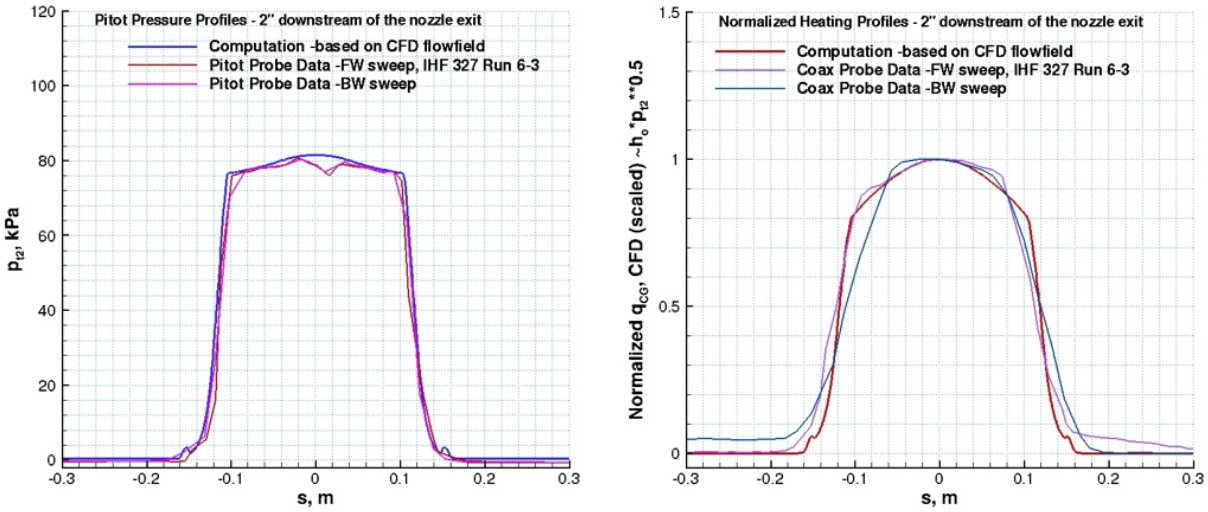

(a) pitot pressure **(b) normalized heat flux**

Figure 8. Comparisons of computations with the pitot pressure and coaxial gage heat flux survey data at x_{ml} = 5.08 cm location. IHF 9-inch nozzle flow: $\dot{m}$ = 849 g/s, h_{ob} = 21.4 MJ/kg, h_{ocl} = 24.2 MJ/kg, parabolic enthalpy profile, 6.4% Ar, p_{box} = 2 torr.

C. IHF 9-inch nozzle flow/20° wedge model simulations

First, CFD flowfield simulations for the wedge model with the water-cooled calibration plate are presented, including comparisons with the calibration plate pressure and heat flux data. CFD simulations for the wedge model with the RCG-coated tile calibration plate follow.

i. Simulations of the 20° wedge model with the water-cooled calibration plate

During IHF 335 tests, the panel test articles installed on the wedge model were tested at three conditions. Here, the results for one condition will be presented in detail, and for the other two conditions only summaries of CFD results will be given. IHF 335 condition 3 represents a facility condition similar to IHF 327 condition 3: near the facility maximum in terms of arc heater mass flow rate and arc current, and it includes minimal cold-gas injection at the plenum.

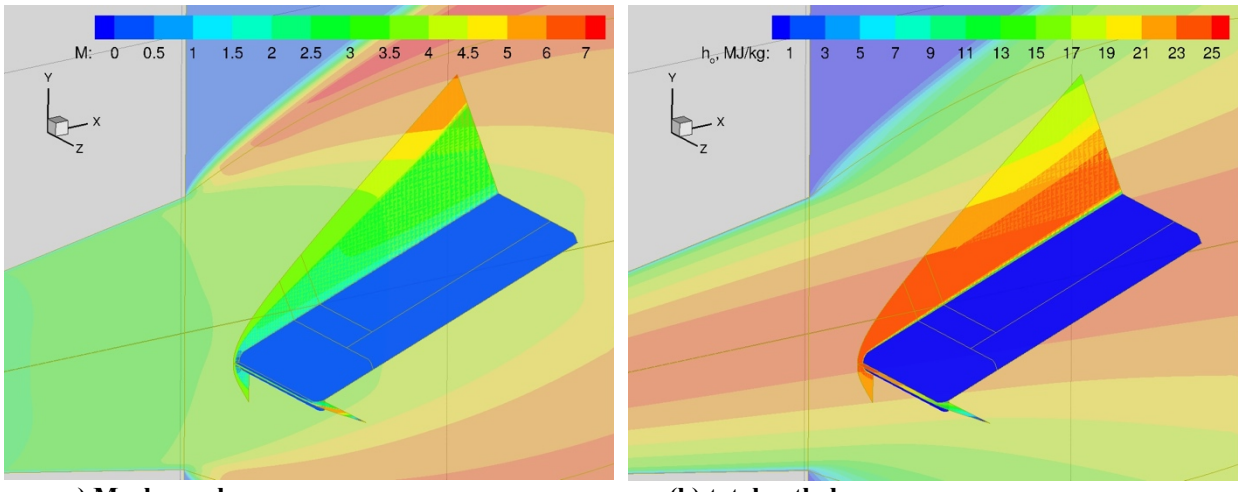

a) Mach number **(b) total enthalpy**

Figure 9. Computed flowfield contours of the IHF 9-inch nozzle flow and test box with the 20° wedge model: $\dot{m}$ = 843 g/s, h_{ob} = 19.0 MJ/kg, h_{ocl} = 24.2 MJ/kg, parabolic enthalpy profile, 6.3% Ar, p_{box} = 2 torr.

Figure 9 shows the computed Mach number and total enthalpy contours of the IHF 9-inch nozzle flow near the nozzle exit and test box with the 20° wedge model at IHF 335 condition 3. The contours are shown on the x-y symmetry planes of the nozzle flowfield and on other planes of interest for the flowfield of the test box and over the wedge model. The wedge model was tested at 5.08 cm downstream of the nozzle exit and at an off-centerline location (the leading edge of the wedge model is about 3.4 cm below centerline), thus reducing the effects of the expansion waves on the model surface quantities.

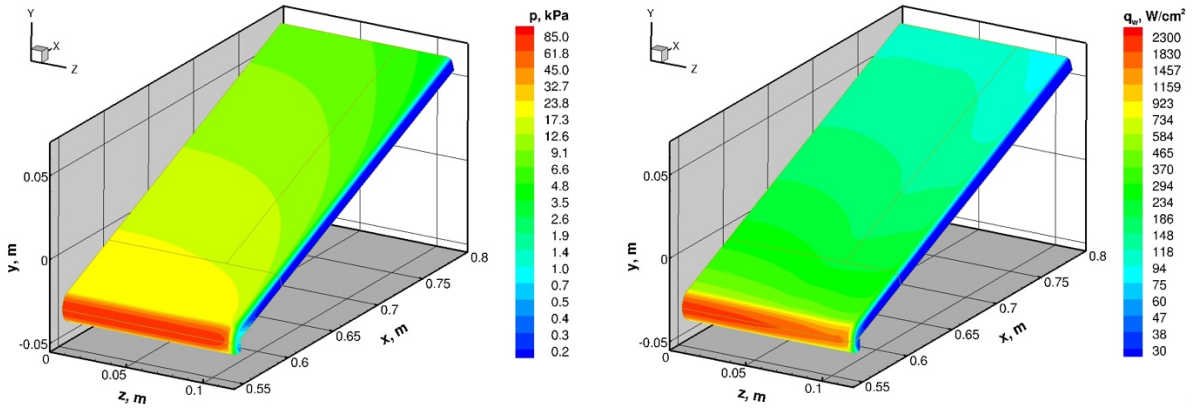

(a) pressure **(b) cold-wall heat flux**

Figure 10. Computed surface quantities of the 20° wedge model with the water-cooled calibration plate. IHF 9-inch nozzle flow: $\dot{m}$ = 843 g/s, h_{ob} = 19.0 MJ/kg, h_{ocl} = 24.2 MJ/kg, 6.3% Ar.

Figure 10 shows contours of the computed surface quantities (pressure and heat flux) of the wedge model with the calibration plate configuration. Note that the surface pressure drops significantly along the wedge centerline. The decrease in pressure along the plate centerline is primarily due to the following two factors: three-dimensional conical flow expansion over the side of the model (cross flow effects), and interaction of the expansion waves from the nozzle exit with the bow shock wave of the wedge model. As expected, the effect of the expansion wave becomes increasingly important when the model size and the nozzle exit diameter are comparable. Note that the nozzle exit diameter is only slightly larger than the width of the wedge model.

Figure 11 shows computed calibration plate surface quantities and comparisons with the measured calibration plate data. The contour plots show computed surface pressure and heat flux on one half of the calibration plate, and the symbols in the contour plots are the measurements, color coded with the same contour levels. A complete uncertainty analysis of the calibration plate measurements is not available. However, based on historical Ames arc-jet data with similar measurements, the heat flux measurements are estimated to be accurate to within ±15% and the pressure measurements to within ±5%. Note that computed and measured surface pressure values are in good agreement. The agreement in the rate of pressure drop along the plate centerline indicates that wave interaction and three-dimensional effects are adequately captured by the CFD simulations. For the heat flux comparisons, the agreement is considered fair. As summarized in Table 2, the calibration plate pressure and heat measurements were remarkably consistent for the five arc-jet runs. Among the heat flux gages along the plate centerline (Q_1, Q_2, Q_3, and Q_4), Q_3 measurements showed the largest discrepancy from the computed trend line in Fig. 11b. It is not clear whether this is related to the flow disturbance observed in the probe survey data of Fig 8. Note that the pressure measurements do not indicate any flow disturbance at all. Between the two off-centerline gages (Q_5 and Q_6), Q_6 measurements were notably higher, but still within the measurement uncertainty.

Table 2 gives a summary of the facility and calibration data obtained in IHF 335 tests for condition 3, and corresponding CFD estimates. The tabulated values of surface pressure, heat flux (CWFC and HWFC), and shear are given for the test plate centerline (not for the calibration plate). The wedge model in the test plate configuration includes a carbon phenolic conditioning plate (2.54 cm or 1 in). Note that CFD simulations of the wedge model with the test plate for HWFC heat flux estimates are not presented; only the results are reported in Table 2. The hot-wall fully-catalytic heat flux predictions are important for flight to arc-jet test traceability purposes since the flight environment definition is usually based on these quantities.

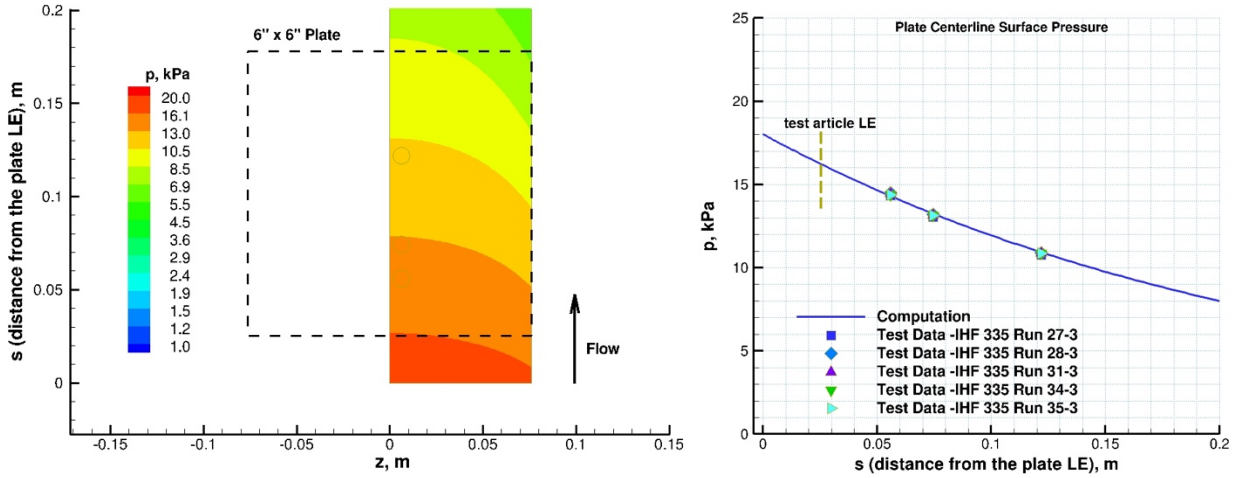

(a) pressure

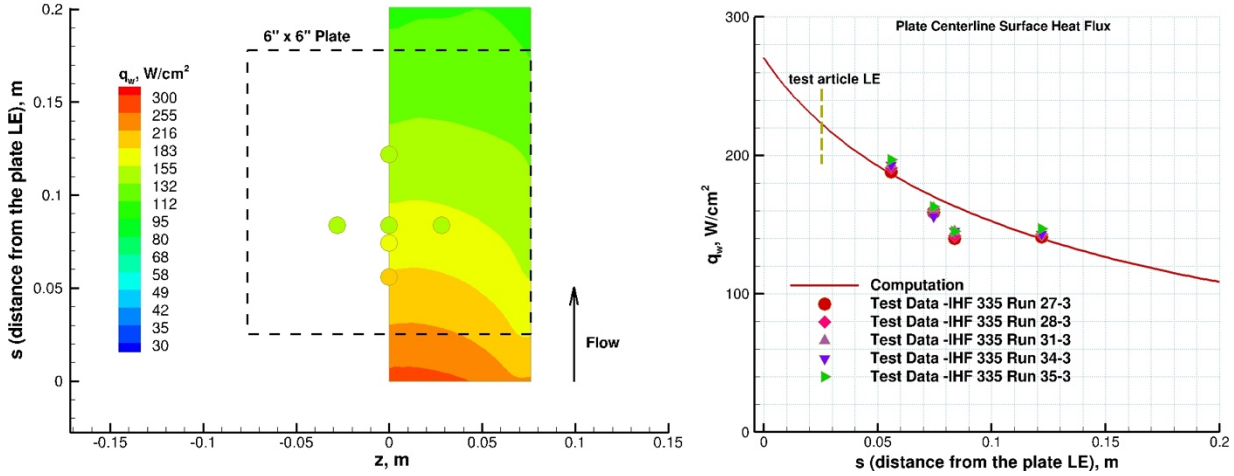

(b) cold-wall heat flux

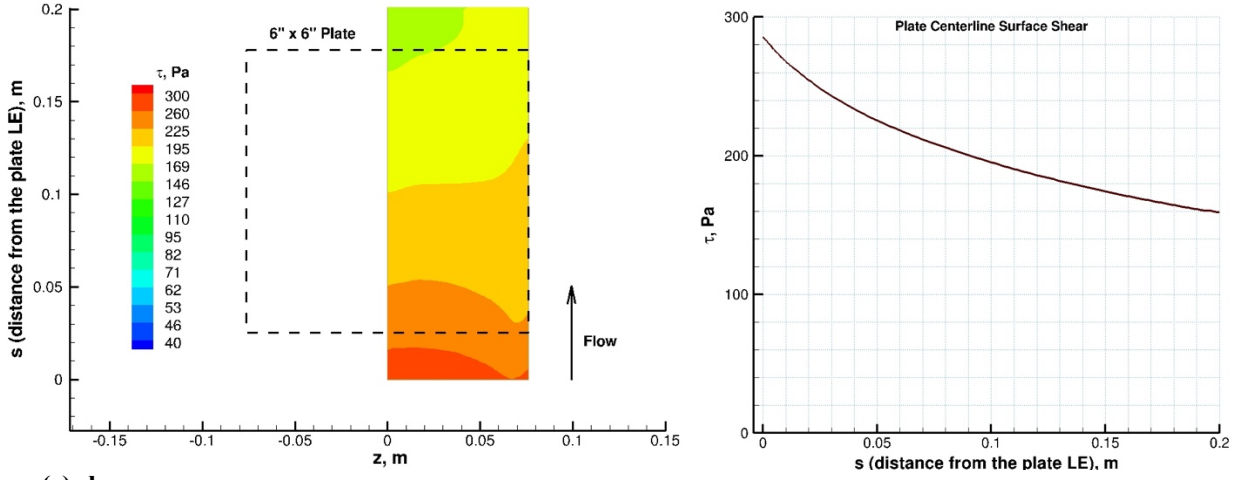

(c) shear

Figure 11. Computed surface quantities of the calibration plate using the 20° wedge model and comparisons with the calibration data. IHF 9-inch nozzle flow: $\dot{m}$ = 843 g/s, h_{ob} = 19.0 MJ/kg, h_{ocl} = 24.2 MJ/kg, 6.3% Ar. Symbols color-coded with the contour colors are the test data from IHF 335 Run 35-3.

Table 2. Summary of facility conditions, stagnation calorimeter and 20° wedge water-cooled calibration plate data obtained in the IHF 9-inch nozzle at x_{ml} = 5.08 cm, and corresponding CFD estimated parameters, IHF 335 condition 3.

	IHF 335 Tests Facility/Calibration Data				
	Run 27-3	**Run 28-3**	**Run 31-3**	**Run 34-3**	**Run 35-3**
p_{ch}, kPa	809	809	817	816	814
I, A	6016	6015	6018	6019	6017
V, V	6597	6602	6652	6644	6626
$\dot{m}$, g/s	843	843	843	843	843
$\dot{m}_m$	740	740	740	740	740
$\dot{m}_a$	50	50	50	50	50
$\dot{m}_{ar}$	53	53	53	53	53
h_{ob} (W), MJ/kg	20.7	20.7	21.3	21.2	21.1
p_1, p_2, p_3, kPa	14.4, 13.1, 10.8	14.5, 13.2, 10.9	14.5, 13.2, 10.9	14.4, 13.1, 10.9	14.5, 13.2, 10.9
Q_5, W/cm^2	150	153	153	153	152
Q_1, Q_2, Q_3, Q_4	188, 159, 140, 141	191, 161, 142, 143	194, 162, 145, 145	193, 156, 145, 143	197, 163, 145, 147
Q_6	144	133	144	143	145
q_{isoq}, W/cm^2	1196	1314		1371	
p_{isoq}, kPa	82.6	82.7		83.6	
	CFD Estimates				
$\dot{m}$, g/s	843				
$c_{Ar,\%}$	6.3				
h_{ob}, MJ/kg	19.0				
h_{ocl}, MJ/kg	24.2				
p_s, kPa	16.2 – 18.7				
q_{CWFC}, W/cm^2	223 – 116				
q_{HWFC}, W/cm^2	181 – 105				
τ_s, Pa	248 – 165				
δ, cm	0.34				
M_e	1.70				
Re_x	1.3x10^4				

CFD-estimated surface quantities are given along the test plate centerline from the leading edge to 15.24 cm downstream.

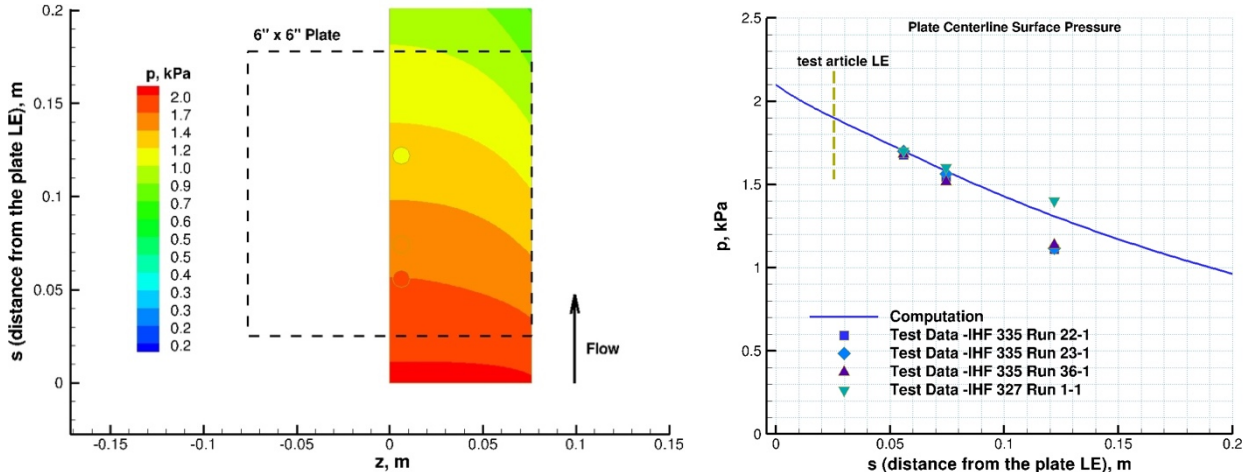

(a) pressure

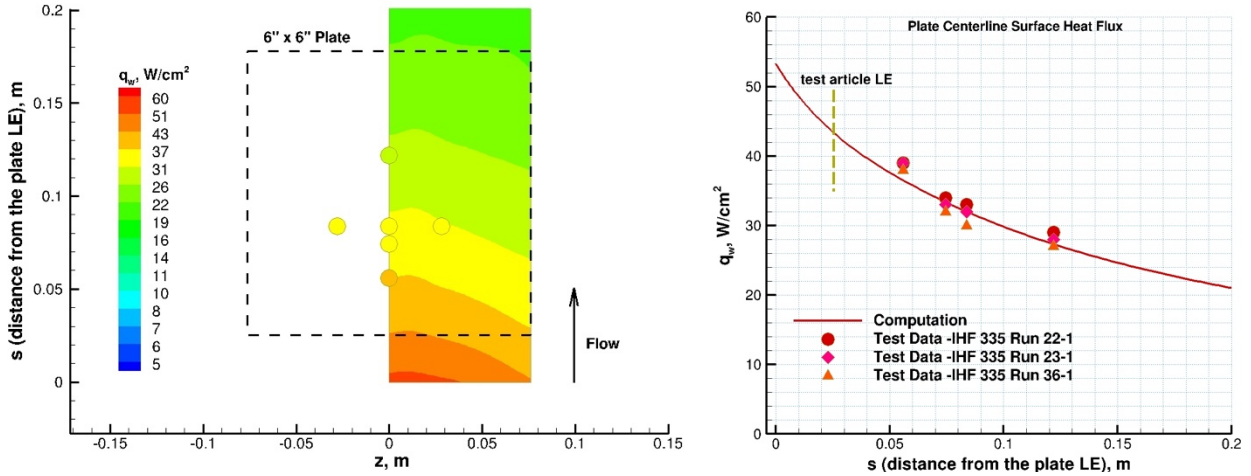

(b) cold-wall heat flux

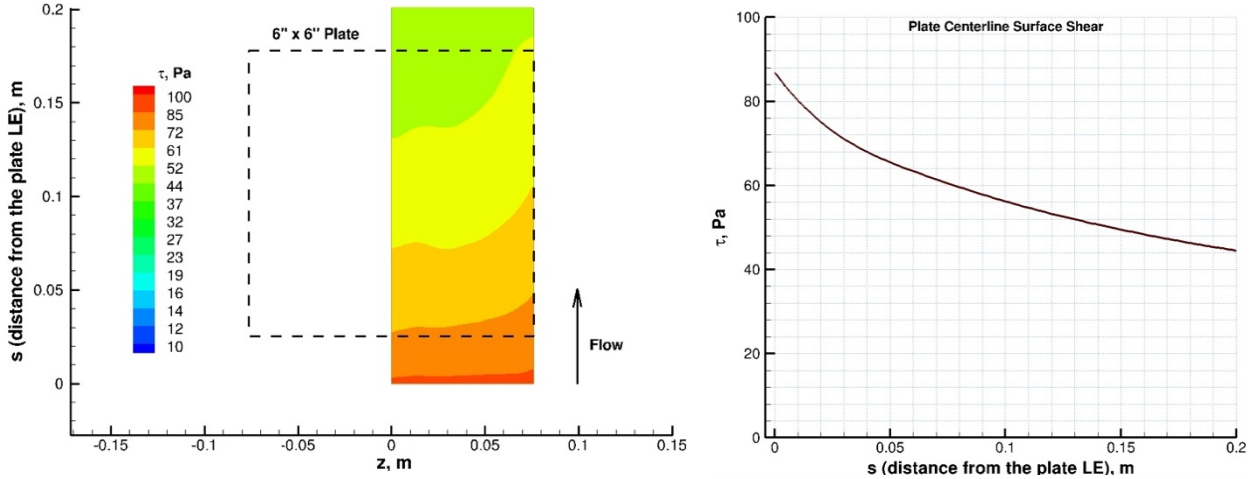

(c) shear

Figure 12. Computed surface quantities of the calibration plate using the 20° wedge model and comparisons with the calibration data. IHF 9-inch nozzle flow: $\dot{m}$ = 144 g/s, h_o= 10.1 MJ/kg, h_{ocl} = 15.4 MJ/kg, 9.7% Ar. Symbols color-coded with the contour colors are the test data from IHF 335 Run 23-1.

Table 3. Summary of facility conditions, data from stagnation calorimeter and two 20° wedge calibration plates obtained at x_{ml} = 5.08 cm location, and corresponding CFD estimated parameters, IHF 335 condition 1.

	IHF 335 Tests Facility/Calibration Data		
	Run 22-1	**Run 23-1**	**Run 36-1**
p_{ch}, kPa	104	104	104
I, A	2037	2037	2035
V, V	2109	2114	2113
$\dot{m}$, g/s	144	144	144
$\dot{m}_m$	80	80	80
$\dot{m}_a$	50	50	50
$\dot{m}_{ar}$	14	14	14
h_{ob} (W), MJ/kg	10.1	10.3	10.1
p_1, p_2, p_3, kPa	1.68, 1.54, 1.11	1.70, 1.56, 1.12	1.69, 1.52, 1.14
Q_5, W/cm^2	34	32	31
Q_1, Q_2, Q_3, Q_4	39, 34, 33, 29	39, 33, 32, 28	38, 32, 30, 27
Q_6	36	35	33
TC_1, TC_7, TC_{13}, K	1340, 1238, 1174	1314, 1242, 1222	
TC_2, TC_8, TC_{14}	1378, 1263, 1183	1345, 1271, 1242	
$TC_3, TC_6, TC_9, TC_{12}, TC_{15}$	1388, 1334, 1264, 1226, 1181	1345, 1316, 1277, 1272, 1248	
TC_4, TC_{10}, TC_{16}	1410, 1289, 1204	1381, 1281, 1240	
TC_5, TC_{11}, TC_{17}	1047, 1269, 1187	1027, 1268, 1221	
q_{isoq}, W/cm^2	217		
p_{isoq}, kPa	10		
	CFD Estimates		
$\dot{m}$, g/s	144		
$c_{Ar,\%}$	9.7		
h_{ob}, MJ/kg	10.1		
h_{ocl}, MJ/kg	15.4		
p_s, kPa	1.90 – 1.04		
q_{CWFC}, W/cm^2	43 – 23		
q_{HWFC}, W/cm^2	36 – 21		
q_{RCG}, W/cm^2	25 – 13		
T_{RCG}, K	1488 – 1275		
τ_s, Pa	73 – 46		
δ, cm	0.70		
M_e	1.81		
Re_x	2.3x10^3		

Table 3 gives a summary of the facility and calibration data for IHF 335 condition 1. Figure 12 shows computed calibration-plate surface quantities and comparisons with the measured calibration plate data for this condition. Although the predicted surface pressures are usually in good agreement with the measurements, within ±5%, for this

case p_3 pressure measurements in the IHF 335 runs are much lower the computed pressure at this location. The slope of the predicted pressure drop appears to be less than that of the measurements. For this reason, the pressure data from IHF 327 Run 1-1 are also plotted in Fig. 12a. Note that the arc heater conditions for IHF 327 condition 1 are similar to those of IHF 335 condition 1, only arc-heater pressure and current are slightly lower. The reason for this large variation in p_3 measurements (or the pressure discrepancy) is not clear. For this case, the heat flux comparisons in Fig. 12b show good agreement; Q_3 measurements did not show the discrepancy discussed earlier in Fig. 11b for the previous case.

Similarly, Table 4 gives a summary of the facility conditions, calibration data, and CFD estimates for IHF 335 condition 2. Figure 13 shows contours and line plots of computed calibration plate surface quantities and comparisons with the test data for this condition. Again, computed pressure and heat flux values are in good agreement with the measurements.

Table 4. Summary of facility conditions, stagnation calorimeter and 20° wedge water-cooled calibration plate data obtained at x_{ml} = 5.08 cm location, and CFD estimated parameters, IHF 335 condition 2.

	IHF 335 Tests Facility/Calibration Data	
	Run 22-2	**Run 23-2**
p_{ch}, kPa	404	403
I, A	2831	2830
V, V	4946	4935
$\dot{m}$, g/s	468	467
$\dot{m}_m$	381	380
$\dot{m}_a$	55	55
$\dot{m}_{ar}$	32	32
h_{ob} (W), MJ/kg	15.9	15.8
p_1, p_2, p_3, kPa	6.7, 6.1, 4.9	6.7, 6.1, 4.9
Q_5, W/cm^2	78	80
Q_1, Q_2, Q_3, Q_4	105, 87, 82, 75	106, 88, 83, 76
Q_6	81	81
q_{isoq}, W/cm^2	562	
p_{isoq}, kPa	40.9	
	CFD Estimates	
$\dot{m}$, g/s	468	
$c_{Ar, \%}$	6.8	
h_{ob}, MJ/kg	14.4	
h_{ocl}, MJ/kg	18.9	
p_s, kPa	7.7 – 4.1	
q_{CWFC}, W/cm^2	117 – 61	
q_{HWFC}, W/cm^2	94 – 55	
τ_s, Pa	163 – 106	
δ, cm	0.42	
M_e	1.75	
Re_x	7.2x10^3	

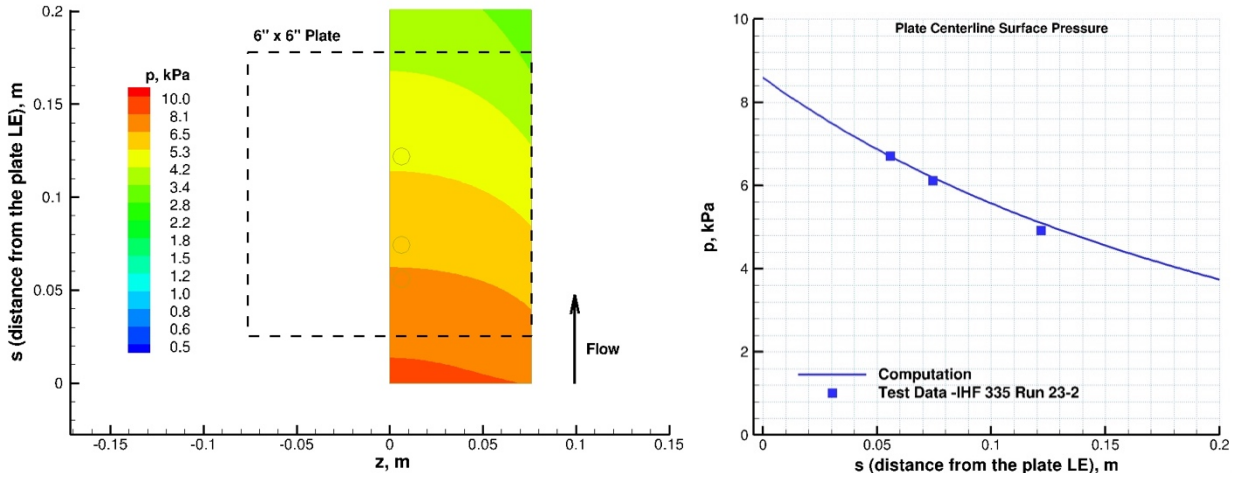

(a) pressure

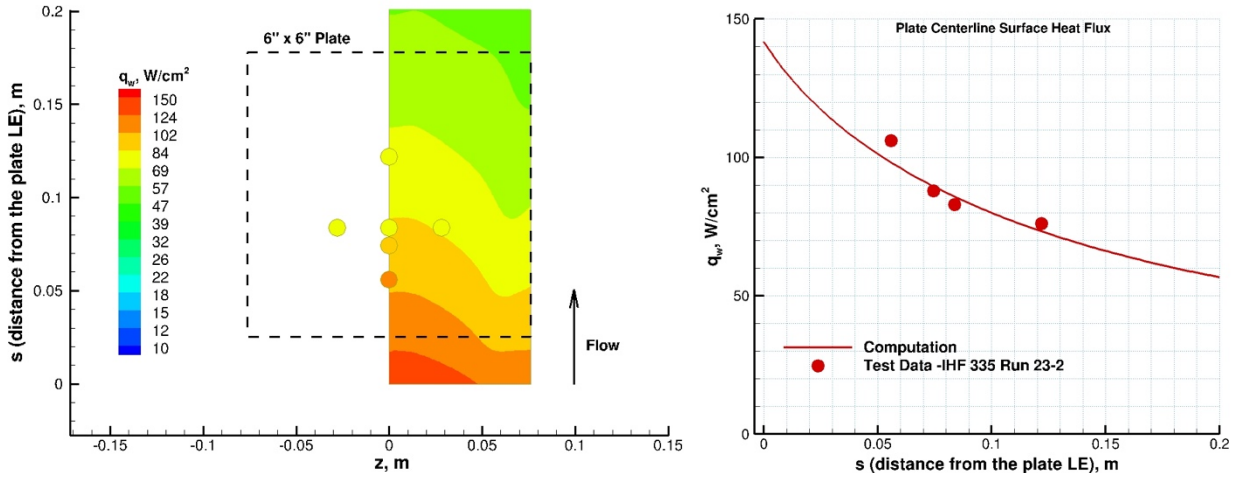

(b) cold-wall heat flux

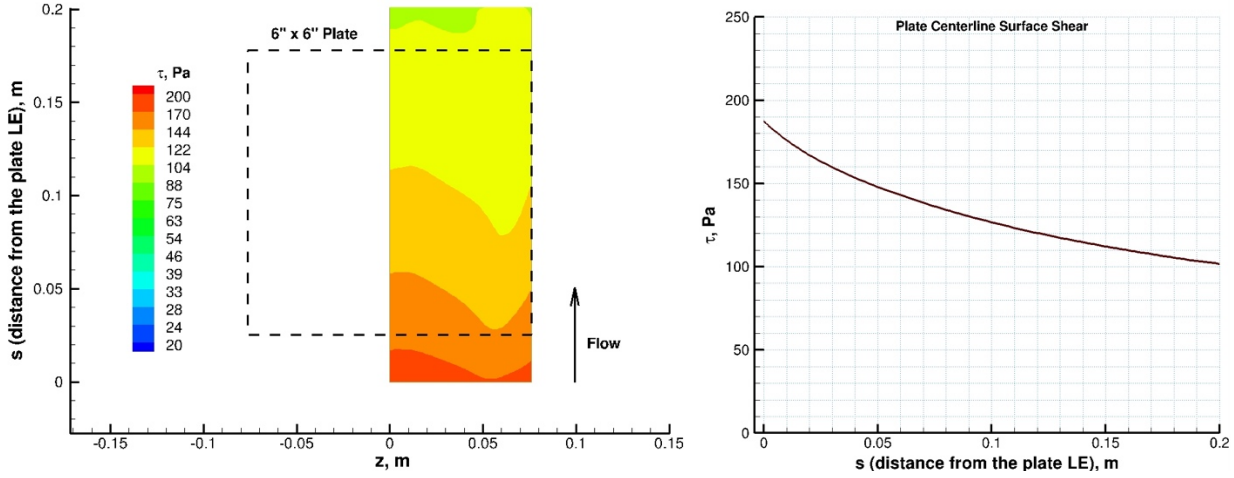

(c) shear

Figure 13. Computed surface quantities of the calibration plate using the 20° wedge model and comparisons with the calibration data. IHF 9-inch nozzle flow: $\dot{m}$ = 468 g/s, h_{ob} = 14.4 MJ/kg, h_{ocl} = 18.9 MJ/kg, 6.8% Ar. Symbols color-coded with the contour colors are the test data from IHF 335 Run 23-2.

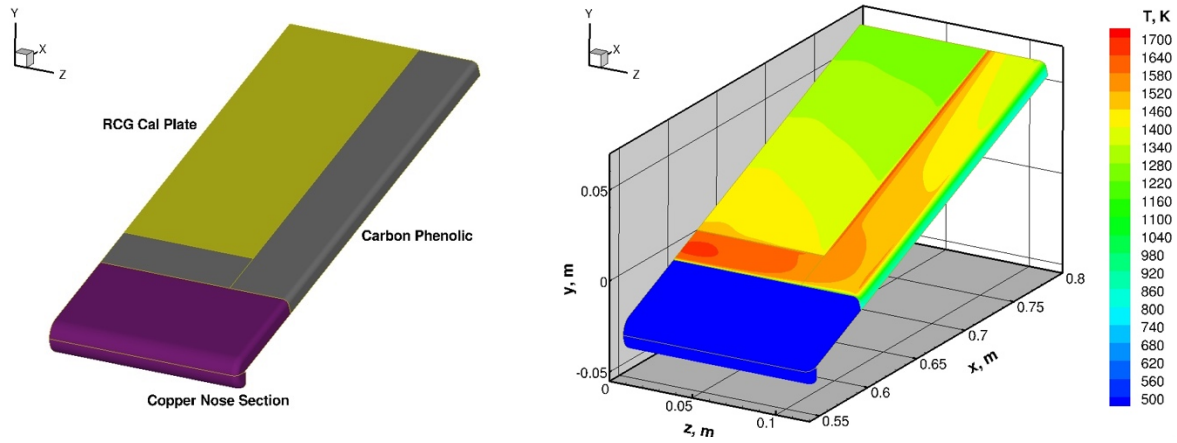

(a) material map **(b) surface temperature**

Figure 14. Computed surface temperature contours of the 20° wedge model with the RCG-coated tile calibration plate. IHF 9-inch nozzle flow: $\dot{m}$ = 144 g/s, h_{ob} = 10.1 MJ/kg, h_{ocl} = 15.4 MJ/kg, 9.7% Ar.

ii. Simulations of the 20° wedge model with the RCG-coated tile calibration plate

As mentioned earlier, an RCG-coated tile plate (Fig. 2b) is also used for calibration and flow characterization purposes at relatively lower heating conditions. Figure 14 shows the wedge material map and computed surface temperature contours of the wedge model in test article configuration with the RCG-coated tile plate. The water-cooled copper sections of the model are assumed to be at 500 K while the carbon phenolic section (side frame and conditioning plate) and the RCG plate temperatures are computed using radiative equilibrium boundary conditions. The conditioning plate and side frame are assumed to be fully catalytic, whereas for the RCG plate, surface catalysis reactions of Stewart [13] are used. The temperature drop going from the conditioning plate to the RCG plate in Fig. 14b is due to much lower catalytic atom recombination efficiencies prescribed for the RCG plate.

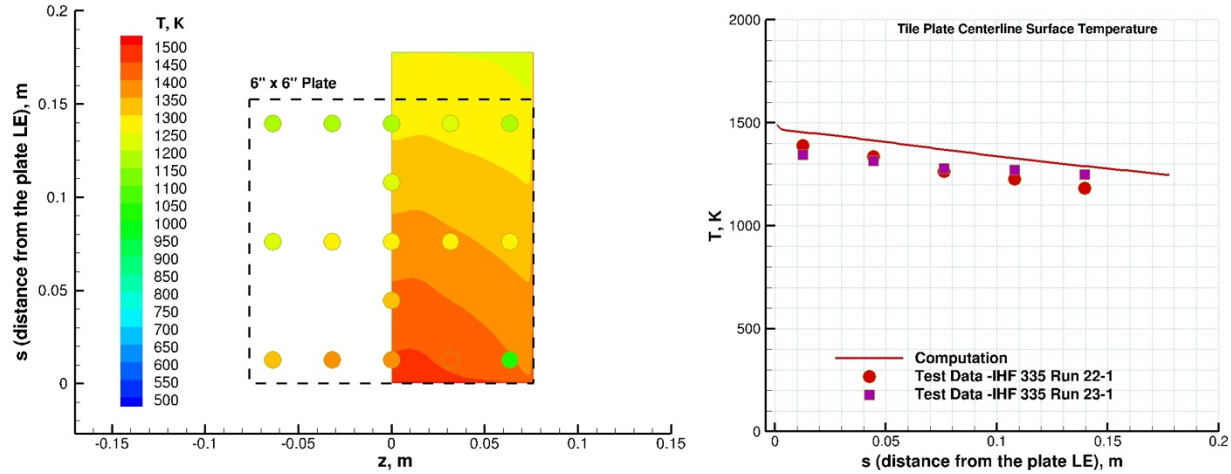

Figure 15. Computed surface temperature contours of the RCG calibration plate and comparisons with the thermocouple data. IHF 9-inch nozzle flow: $\dot{m}$ = 144 g/s, h_o = 10.1 MJ/kg, h_{ocl} = 15.4 MJ/kg, 9.7% Ar. Symbols color-coded with the contour colors are the test data from IHF 335 Run 22-1.

In Fig. 15, contour and line plots of the computed radiative equilibrium surface temperature on the RCG calibration plate are presented with the corresponding test data. As expected, both computed and measured temperatures monotonically decrease along the plate centerline, a trend similar to that of the computed and measured heat fluxes shown in Fig. 12b. The predicted temperatures are lower than the measurements by 40 K to as much as 90 K. As summarized in Table 3, the surface temperature measurements were repeatable between the two runs: at most locations they were within 25 to 35 K for the two runs, and TC_5 measurements were unusually low (this was also observed in

the LEAF tests when the RCG tile plate is used for radiation calibration runs [2]). Also, note that while the computed water-cooled calibration heat flux values presented in the previous section are primarily sensitive to total enthalpy and its distribution, the computed RCG tile surface temperature is additionally sensitive to surface catalysis and surface emissivity. It should be mentioned that since the surface temperature is computed using the radiative equilibrium boundary condition, any in-depth heat conduction would lower the computed surface temperature. However, the heat conduction effects on the computed RCG-coated tile surface temperature are investigated in [17] and found to be relatively small.

Finally, CFD-estimated test environment parameters presented here are used for material response analyses of the test articles in the LEAF wedge tests. The material performance results of the LEAF wedge tests will be presented in a separate paper [18].

D. Computational grid details and estimated uncertainties

The two-dimensional axisymmetric and three-dimensional CFD computations of the IHF 9-inch nozzle flowfields, including the test box and models, were performed using multi-block grids. All computational grids were generated using a commercial software package, *Gridgen* [19]. For the axisymmeric IHF 9-inch nozzle simulations with stagnation calorimeter models, 114,900 cells were used; the number of cells from the nozzle inlet to the nozzle exit was 480, with 120 cells normal to the wall along the nozzle. For the three-dimensional IHF 9-inch nozzle/test box flowfields, 13.93 million cells were used. For the 20° wedge models, with the water-cooled calibration plate or the RCG tile plate, the grid sizes were 3.60 million cells. Based on a limited number of grid refinement studies, grid quality issues of the computations and numerical accuracy are adequately addressed.

CFD computations of arc-jet flows, as for hypersonic flight simulations, include uncertainties in many of the model input parameters. It is not possible at this time to do a complete uncertainty analysis of computed results for all of the simulation input parameters. The most important input parameter of the arc-jet test flow is the total enthalpy and its distribution at the nozzle inlet. Noting that the centerline total enthalpies used in CFD simulations rely on calorimeter data, calibration plate measurements, facility data, and other modeling input parameters, the uncertainty in the heat flux predictions for the wedge calibration plates is estimated to be as much as ±20%, and the uncertainty in the surface pressure predictions is estimated to be ±5-10%.

Uncertainty analyses of surface pressure, heat flux and temperature measurements are also not available at this time. However, both heat flux measurements, i.e., using slug calorimeters [20] and Gardon gages on a water-cooled calibration plate [21], are standard facility measurements for arc-jet tests. Based on empirical evidence (historical Ames arc-jet data), the heat flux measurements are estimated to be accurate to within ±15% and the pressure measurements to within ±5%. The thermocouple devices are estimated to be accurate to within ±1-2%; if the measurement errors related to the thermocouple installations are included, they could be as much as ±4%.

VI. Summary and Concluding Remarks

Computational simulations in support of LEAF wedge tests in the NASA Ames 60-MW Interaction Heating Facility flow are presented. These tests were conducted using a wedge model placed in a free jet downstream of the IHF 9-inch nozzle. Both the nozzle and wedge model are specifically designed for testing in the new Laser-Enhanced Arc-jet Facility. The calibration data included heat flux and pressure measurements with stagnation calorimeters, measurements of surface pressure and heat flux on a water-cooled calibration plate, and surface thermocouple measurements on an RCG-coated tile plate. The two instrumented calibration plates were both integrated with the wedge model. Experimental surveys of arc-jet test flow with pitot and heat flux probes were also performed at three arc-heater conditions, providing assessment of the flow uniformity and valuable data for the flow characterization.

The probe surveys, covering a range of conditions from one at the minimum current and mass flow rate to one at the near facility maximum, indicate a varying degree of flow nonuniformity in the test flow. The present CFD simulations approximately reproduce the measured sweep data at these three conditions. For the LEAF wedge tests, computations of the nonequilibrium flowfield in the nozzle, test box, and over the test articles are performed. These CFD simulations predict model surface pressure and heat flux measurements reasonably well, consistent with the set of arc-jet facility data and taking into account nonuniform total enthalpy and mass flux profiles at the nozzle inlet as

well as the expansion waves emanating from the nozzle exit and their effects on the model flowfields. Through comparisons with the test data, the presented CFD simulations yield estimates of the arc-jet test environment parameters that are needed to evaluate the performance of thermal protection system materials. These estimated parameters include centerline total enthalpy, surface shear, hot-wall heat flux, boundary layer thickness, and boundary layer edge Mach number.

As demonstrated in our previous work for other Ames arc-jet facilities, CFD simulations, when supported with the experimental evidence, define arc-jet test environments along with valuable insights and ultimately provide a framework for tracing a TPS material performance from a ground test facility to flight.

Acknowledgments

This work was funded by the NASA Orion TPS Insight/Oversight project. The arc-jet operational capability at NASA ARC is also supported by NASA-SCAP. The authors would like to thank the LEAF-Lite project for providing IHF 327 test data, in particular, G. Joseph Hartman, John A. Balboni, Daniel Philippidis, and TSF test engineers involved in Orion TPS/LEAF-Lite tests, Frank C. L. Hui, J. Enrique Carballo, and Imelda Terrazas-Salinas. The support from the NASA Ames Entry Systems and Technology Division, through contract NNA15BB15C to AMA, Inc., is gratefully acknowledged.

References

[1] Terrazas-Salinas, I., and the staff of Thermophysics Facilities Branch, "Test Planning Guide for NASA Ames Research Center Arc-Jet Complex and Range Complex," A029-9701-XM3 Rev. D, Entry Systems and Technology Division, NASA Ames Research Center, January 2018.

[2] Cushman, G., Alunni, A., Balboni, J., Zell, P., Hartman, J., and Empey, D. M., "The Laser Enhanced Arc-Jet Facility (LEAF-Lite): Simulating Convective and Radiative Heating with Arc-jets and Multiple 50-kW CW Lasers," AIAA Paper 2018-3273, June 2018.

[3] Fretter, E., "Interaction Heating Facility (IHF) Fact Sheet," http://www.nasa.gov/centers/ames/thermophysics-facilities-home, Thermophysics Facilities Branch, Entry Systems and Technology Division, NASA Ames Research Center, Sept. 2016.

[4] Terrazas-Salinas, I., Carballo, J. E., Driver, D. M., and Balboni, J. A., "Comparison of Heat Transfer Measurement Devices in Arc Jet Flows with Shear," AIAA Paper 2010-5053, June 2010.

[5] Driver, D. M., Hartman, J., Philippidis, D., Noyes, E., Hui, F., and Terrazas-Salinas, I., "Evidence of Standing Waves in Arc Jet Nozzle Flow," AIAA Paper 2017-4452, June 2017.

[6] Wright, M. J., Candler, G. V., and Bose, D., "Data-Parallel Line Relaxation Method for the Navier-Stokes Equations," *AIAA Journal*, Vol. 36, No. 9, 1998, pp. 1603-1609.

[7] Wright, M. J., "Data-Parallel Line Relaxation Code, DPLR Version 4.02," Private Communication, June 2010.

[8] Park, C., *Nonequilibrium Hypersonic Aerothermodynamics*, John Wiley & Sons, Inc., New York, 1990, Chap. 4.

[9] Gökçen, T., Chen, Y. K., Skokova, K. A., and Milos, F. S., "Computational Analysis of Arc-Jet Stagnation Tests Including Ablation and Shape Change," *Journal of Thermophysics and Heat Transfer*, Vol. 24, No. 4, 2010, pp. 694-707; also AIAA Paper 2009-3596, June 2009.

[10] Gökçen, T., Balboni, J. A., and Alunni, A. I., "Computational Simulations of the 10-MW TP3 Arc-Jet Facility," AIAA Paper 2015-3103, June 2015.

[11] Gökçen, T., and Alunni, A. I., "Flow Characterization Studies of the 10-MW TP3 Arc-Jet Facility: Probe Sweeps," AIAA Paper 2016-4153, June 2016.

[12] Gökçen, T., and Skokova, K. A., "CFD Simulations of the IHF Arc-Jet Flow: Compression-Pad/Separation Bolt Wedge Tests," AIAA Paper 2017-4451, June 2017.

[13] Stewart, D. A., "Surface Catalysis and Characterization of Proposed Candidate TPS for Access-to-Space Vehicles," NASA TM-112206, July 1997.

[14] ASTM E637-05, "Standard Test Method for Calculation of Stagnation Enthalpy from Heat Transfer Theory and Experimental Measurements of Stagnation-Point Heat Transfer and Pressure," American Society for Testing and Materials, November 2005 (originally published in 1978).

[15] Gökçen, T., "Effects of Test Box Pressure on Arc-Jet Flowfields and Implications for Testing," AIAA Paper 2018-3771, June 2018.

[16] Winovich, W., "On the Equilibrium Sonic-Flow Method for Evaluating Electric-Arc Air-Heater Performance," NASA TN-D-2132, March 1964.

[17] Gökçen, T., Alunni, A. I., Skokova, K. A., Chen, Y-K., and Empey, D. E., "Analysis of Arc-Jet Tile Calibration Tests in the PTF: Compression-Pad Surface Heating Distribution," AIAA Paper 2014-2816, June 2014.

[18] Alunni, A. I., Gökçen, T., and Boghazian, T., "LEAF Wedge Tests: Avcoat Material Performance Under Convective and Radiative Heating Environments," Extended abstract submitted for Thermophysics at AIAA SciTech Conferences, January 6-10, 2020.

[19] "Gridgen, Version 15.17," Pointwise, Inc., Fort Worth, TX.

[20] ASTM E457-96, "Standard Test Method for Measuring Heat-Transfer Rate Using a Thermal Capacitance (Slug) Calorimeter," American Society for Testing and Materials, Ocober 1996 (Reapproved 2002, originally published in 1972).

[21] ASTM E511-07, "Standard Test Method for Measuring Heat Flux Using a Copper-Constantan Circular Foil Heat-Flux Gage," American Society for Testing and Materials, December 2007 (original standard published in 1973).